X-point potential well formation in diverted tokamaks with unfavorable magnetic field direction

**M. Wensing[1], J. Loizu[1], H. Reimerdes[1], B. P. Duval[1],
M. Wischmeier[2] and the TCV team[3]**

[1]École Polytechnique Fédérale de Lausanne (EPFL), Swiss Plasma Center (SPC),
CH-1015 Lausanne, Switzerland,
[2]Max Planck Institut für Plasmaphysik, Boltzmannstr. 2, 85748 Garching, Germany
[3]See author list of S. Coda et al 2019 Nucl. Fusion 59 112023

E-mail: `mirko.wensing@epfl.ch`

19 February 2020

Abstract. Fluid simulations of the boundary of fusion plasmas predict the formation of an electric potential well in the vicinity of the X-point in detached divertor conditions with B_t in the unfavorable direction for H-mode access. This potential well arises when the parallel current in the divertor is dominated by Pfirsch-Schlüter currents and is closely related to previously reported potential hill formation in favorable B_t direction. A simple analytic model describes its dependence on plasma shape and divertor conditions. The poloidal particle transport in the divertor is dominated by the parallel flow, while cross-field particle transport in the vicinity of the separatrix is argued to be $E \times B$-dominated, even in the presence of turbulence. With a potential well, the $E \times B$-flow differs qualitatively from the classic drift pattern with the near-SOL poloidal $E \times B$-flux enhanced and reversed while radially widening/compressing the outer/inner divertor leg, respectively.

1. Introduction

Electric fields are one of the main drives for transport in the tokamak edge as flows due to the equilibrium $E \times B$-drift can be of similar magnitude to parallel and turbulent cross-field flows and thereby impact power and particle sharing between the divertor legs [1, 2, 3, 4] and divertor impurity retention [5]. $E \times B$ flow shear can suppress edge turbulence, e.g. possibly contributing to the L-H transition [6]. A correct description of the electric potential ϕ is, hence, of crucial importance in understanding transport in the plasma edge of fusion devices. Previous works on drifts often focused on in-out asymmetries of ion flux and heat loads on the divertor targets for various tokamaks: EAST [7, 8], C-Mod [9], DIII-D [2, 10], ASDEX Upgrade [11], TCV [12] with less attention to the underlying electric potential. Recent studies in forward magnetic field direction for detached divertor conditions show strong poloidal electric fields [3, 13] and the formation of a "potential hill" below the X-point [14], whereas experiments with reversed magnetic field show a significant reduction of the X-point potential [15]. For the first time, we predict a reversal of the poloidal electric field in deeply detached, reversed field conditions on the basis of 2D fluid simulations. These results are reproduced and interpreted using a simple analytic model revealing dependencies on divertor geometry and conditions. It is demonstrated that the divertor $E \times B$ flow can now differ substantially from the classical drift pattern and contribute significantly to particle transport.

The parallel electric field on the open field lines of the scrape-off layer (SOL) is generally determined by the target sheath boundary condition, charge conservation and the parallel electron momentum balance ($Z_{eff} = 1$)[16]

$$E_{\parallel} = \eta_{\parallel} j_{\parallel} - \frac{\nabla_{\parallel}(n_e T_e)}{e n_e} - 0.71 \frac{\nabla_{\parallel} T_e}{e}. \quad (1)$$

As stated in [3], for well-attached plasma conditions ($T_e \gg 2$ eV), the first term in equation 1 can often be neglected as the Spitzer resistivity $\eta_{\parallel}$ scales with $T_e^{-3/2}$. As pressure gradients are typically weak in attached conditions, integration of equation 1 yields that the electric potential ϕ in the SOL is proportional to T_e, leading to the classical estimate for the $E \times B$-drift pattern reviewed in [1, 4]. However, for a sufficiently low temperature, the parallel electric field is determined by a simple Ohm's law $E_{\parallel} = \eta_{\parallel} j_{\parallel}$, with $j_{\parallel}$ determined by the charge balance $\nabla \cdot \mathbf{j} = 0$ and the boundary conditions at the target plates [17, 3]. Generally, $\mathbf{j}$ includes contributions from the diamagnetic drift, viscosity, inertia, ion-neutral friction, polarization current and the above stated parallel current. The non-divergent-free part of the diamagnetic current is denoted as $\tilde{j}_{dia}$ as done in [18] and relates to the ∇B-drift. For a lower single null (LSN) configuration, $\tilde{j}_{dia}$ is directed towards the PFR when B_t is directed clockwise, viewed from above (forward field direction, Figure 1a), and reverses with B_t (Figure 1b). In the absence of compensating cross-field fluxes, such as a turbulent polarization current or ion-neutral current, local charge balance in the PFR is established through parallel currents (cf. [1, 19]). For a low temperature divertor, these parallel currents can, as will be shown, only be driven by an electric field directed from the target plates towards the X-point (cf. Figure 1b). Equivalently, the electric potential at the X-point must remain well below that at the target, $\phi_{XP} < \phi_t$, which is referred to as a potential well in the following.
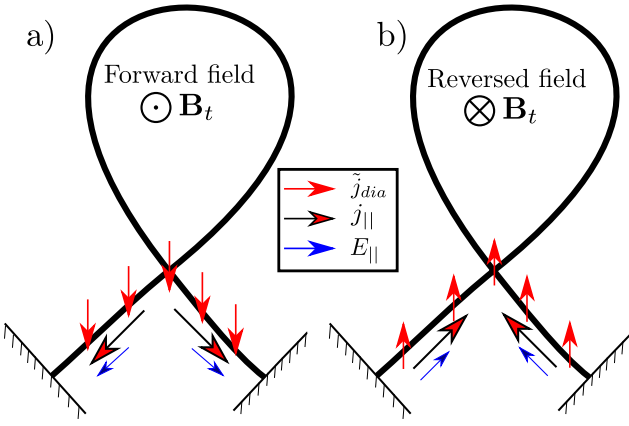
Figure 1. Schematic current and electric field pattern in a) forward ($B_t > 0$) and b) reversed magnetic field ($B_t < 0$) projected to the poloidal plane. PFR parallel current establishes to compensate diamagnetic current contribution.

2. Electric potential well formation

2.1. SOLPS-ITER simulations

In this letter, the electric potential well is studied using 2D scrape-off layer simulations employing the SOLPS-ITER code [20, 21], providing the first reported full drift simulations that include both kinetic neutrals and carbon impurities for the TCV tokamak. Including drift effects in TCV simulations was achieved after recent numerical stability and speed enhancements [22]. The code solves the drift-reduced Braginskii equations, neglecting the time-dependent polarization current (which precludes fluid instability growth) and mimicking the turbulent particle and heat transport with effective diffusive terms. Turbulence simulations, however, indicate a weak time-averaged contribution of the polarization current to the charge balance if the SOL is sufficiently broad, as $\langle \nabla \cdot j_{pol} \rangle / \langle \nabla \cdot j_{dia} \rangle \sim \rho_s / \lambda_p$, where ρ_s is the ion Larmor radius and λ_p the equilibrium pressure fall-off length in the SOL [23, 24]. Typical simulation parameters for TCV are summarized in [25] that yield reason-

able agreement with several diagnostics [26]. The electric potential in forward field simulations follows the classical picture, i.e. $E_{||} = -\nabla_{||}\phi$ directed towards the target and E_r away from the separatrix (Figure 2a-c). However, in the reverse field configuration, a well-resolved region below the X-point of negative electric potential ϕ with respect to the target plates emerges at high densities (Figure 2d-f). Here, $E_{||}$ points towards the target for the common flux region, as expected for regions with low Spitzer resistivity (equation 1) whereas in the PFR, $E_{||}$ is directed towards the X-point. The potential well implies strongly enhanced E_r near the separatrix.
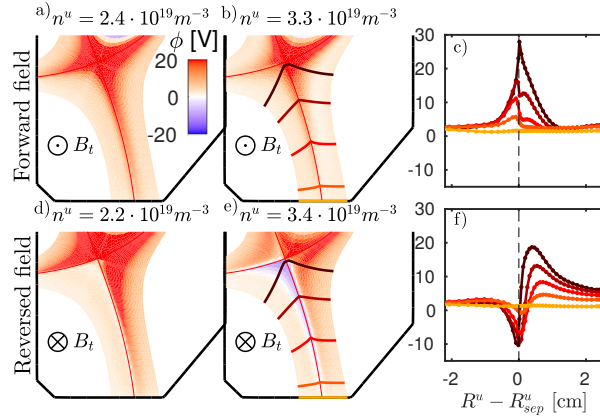
Figure 2. Electric potential ϕ in the divertor in forward (a-c) and reversed field (d-f). For the high density cases the radial ϕ profile for different poloidal locations is shown (c,f). The potential well emerges at high upstream densities in reversed B_t cases. R^u denotes the major radius at the outer midplane.

2.2. Analytic model

The simulations identify the parallel and diamagnetic currents as the main contributors to the charge balance and, therefore, the deduced electric potential ϕ (Figure 3). Other currents are calculated to have smaller contributions to the total divergence (see Table 1). For a detailed description of the various
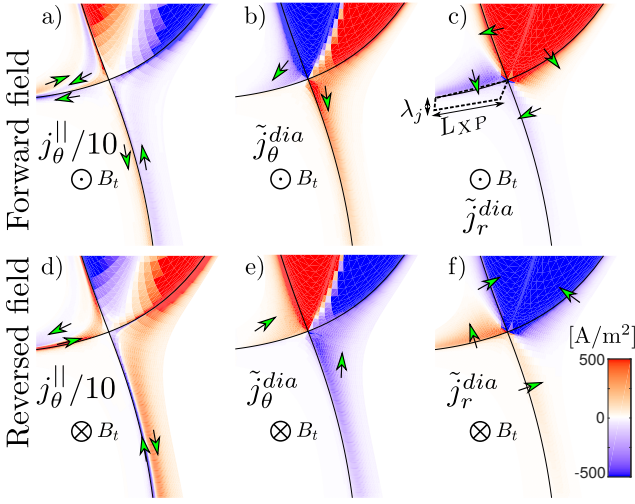
Figure 3. Simulated parallel and diamagnetic current at $n_{ff}^u = 2.4 \cdot 10^{19}$ m^{-3}, $n_{rf}^u = 2.2 \cdot 10^{19}$ m^{-3}.

charge balance contribution [A]	Forward B_t	Rev. B_t
$\int_V \nabla \cdot \mathbf{j}_{\parallel} dV$	102.1	-118.6
$\int_V \nabla \cdot \tilde{\mathbf{j}}_{dia} dV$	-92.5	108.1
$\int_V \nabla \cdot \mathbf{j}_{inert} dV$	-11.0	8.4
$\int_V \nabla \cdot \mathbf{j}_{ion-neutr.} dV$	1.3	0.7
$\int_V \nabla \cdot \mathbf{j}_{vis-\parallel} dV$	0.2	0.9
$\int_V \nabla \cdot \mathbf{j}_{anm.} dV$	< 0.1	< 0.1
$\int_V \nabla \cdot \mathbf{j}_{vis-\perp} dV$	< 0.1	< 0.1

Table 1. Contributions in the SOLPS-ITER simulation to the divergence of electric current in the outer divertor for $n_{ff}^u = 2.4 \cdot 10^{19}$ m^{-3}, $n_{rf}^u = 2.2 \cdot 10^{19}$ m^{-3}. The charge balance is dominated by parallel and diamagnetic currents $\nabla \cdot \mathbf{j}^{\parallel} \approx -\nabla \cdot \mathbf{j}^{dia}$.

currents see [18], section 2.1.2. Leveraging this result, a simple analytic model is proposed that accounts only for parallel and diamagnetic currents in order to determine the average electric field in the PFR of a straight divertor leg, tilted horizontally at an angle α, of a LSN configuration, neglecting the variation of the flux expansion within the leg. A coordinate s is introduced, aligned with the magnetic field line and pointing from the inner to the outer target ($\mathbf{e}_s = \mathbf{e}_{\parallel} \cdot sign(B_\theta)$), i.e. independently of the poloidal magnetic field direction, to

facilitate comparison with simulations using the same sign convention. The parallel current is obtained from equation 1 and the non-divergence-free component of the diamagnetic current is evaluated analytically

$$\mathbf{j}_{\parallel} = \frac{sign(B_\theta)}{\eta_{\parallel}} \left(\frac{\partial_s p}{e n_e} + 0.71 \frac{\partial_s T_e}{e} + E_s \right) \mathbf{e}_s, \quad (2)$$

$$\tilde{\mathbf{j}}_r^{dia} = -B_t p \left(\partial_\theta \frac{1}{B^2} \right) \mathbf{e}_r = -\frac{2p}{B_t^0 R_0} \cos\alpha \, \mathbf{e}_r, \quad (3)$$

where the assumption of a straight divertor leg $\partial_\theta = \cos\alpha \partial_R$ is used. $\mathbf{e}_r$ denotes the cross-field direction in the poloidal plane so the diamagnetic term points into the PFR, $-\mathbf{e}_r$, for $B_t > 0$ (forward field) and away for reversed field. We consider the charge balance equation $\nabla \cdot \mathbf{j} = 0$ within a closed volume extending from the target to the X-point (width L_{XP}, height λ_j) in the PFR enclosing the region where $j_{\parallel}$ does not change sign (cf. Figure 3c). Integration yields

$$\mp j_\theta^{\parallel,t} \lambda_j + \tilde{j}_r^{dia} L_{XP} = \mp j_\theta^{\parallel,XP} \lambda_j, \quad (4)$$

where $j_\theta^{\parallel} = \mathbf{j}_{\parallel} \cdot \mathbf{e}_\theta = j_{\parallel} B_\theta / B$ and the upper/lower signs correspond to the inner/outer divertor legs, respectively. The term $j_{\parallel,XP}$ represents charge sharing between the divertor legs, e.g. by thermo-electric currents which may arise due to asymmetries in the temperature or density between the two targets [27]. Here, the poloidal component of the diamagnetic current is neglected as $j_\theta^{\parallel} \gg \tilde{j}_\theta^{dia}$. Substituting equations 2 and 3 in equation 4 and solving for E_s yields

$$E_s = \eta_{\parallel}(j^{PS} + j^{\parallel,XP}) - \frac{\partial_s p_e}{e n_e} - 0.71 \frac{\partial_s T_e}{e}, \quad (5)$$

$$j^{PS} = \mp \frac{2p}{B_t^0 R_0} \frac{L_{XP}}{\lambda_j} \left| \frac{B_\theta}{B} \right| \cos\alpha, \quad (6)$$

where we identified j^{PS} as the Pfirsch-Schlüter current, i.e. the part of the parallel current which closes the diamagnetic current.

A few key aspects of this simple model should be noted: First, the Pfirsch-Schlüter

contribution to equation 5 becomes important when the parallel resistivity, $\eta_{\|}^{Spitzer} \propto T_e^{-3/2}$, is high, e.g. for detached divertor conditions at low T_e^t, while the classic $E_{\|}$ is recovered at high T_e^t. Second, it allows for ϕ well formation in reversed field $(B_t^0 < 0)$ whereas the classical electric field is amplified in forward field, corresponding to potential hill formation. Third, the term $\eta_{\|} j^{\|,XP}$ inhibits the formation of a Pfirsch-Schlüter-type potential structure as it contributes with equal sign to both divertor legs. Hence, a necessary condition for potential well/hill formation is $|j^{PS}| > |j^{\|,XP}|$.

In the following, we consider the case of negligible current sharing between the divertor legs, i.e. $j^{\|,XP} = 0$ which holds for the TCV simulations (cf. Figure 3a,d). We can obtain a scaling of the potential depth, $\delta\phi \equiv \phi^t - \phi^{XP}$, with divertor conditions and machine size by further approximating the pressure gradient $\frac{\partial_s p}{e n_e} \sim \pm \frac{p_e^{XP}}{e n_e^{XP} L_{XP}} \left|\frac{B_\theta}{B}\right| \approx \pm \frac{T_e^{XP}}{e L_{XP}} \left|\frac{B_\theta}{B}\right|$ and analogously for the temperature and potential gradients. We obtain

$$\frac{e\delta\phi}{T_e^{XP}} \approx \frac{2 e n_e^{XP} \eta_{\|}^t}{B_t^0} \frac{L_{XP}^2}{R_0 \lambda_j} \left|\frac{B}{B_\theta}\right|^2 \cos\alpha + 1.71, \quad (7)$$

$$= m \times \frac{n_e^{XP} [10^{19} m^{-3}]}{(T_e^t [eV]^{3/2})} + 1.71 \quad (8)$$

with $m \approx 1.6 \cdot 10^{-4}\ \Omega m \frac{\ln\Lambda}{B_t^0[T]} \frac{L_{XP}^2}{R_0 \lambda_j} \left|\frac{B}{B_\theta}\right|^2_t \cos\alpha$.

Comparison of analytic model equations 5 and 8 to the 2D simulation is performed by calculating the average electric field between target and X-point. The diamagnetic contributions to equation 5 acting over the leg are evaluated from the X-point parameters (superscript XP) with the parallel contributions evaluated at the target (superscript t). For the simulated TCV discharge $(B_t^0 = 1.44$ T, $R_0 = 0.88$ m, taking Coulomb logarithm $\ln\Lambda \approx 10)$, Table 2 summarizes the parameters. While the model (equation 5, 8) overestimates absolute
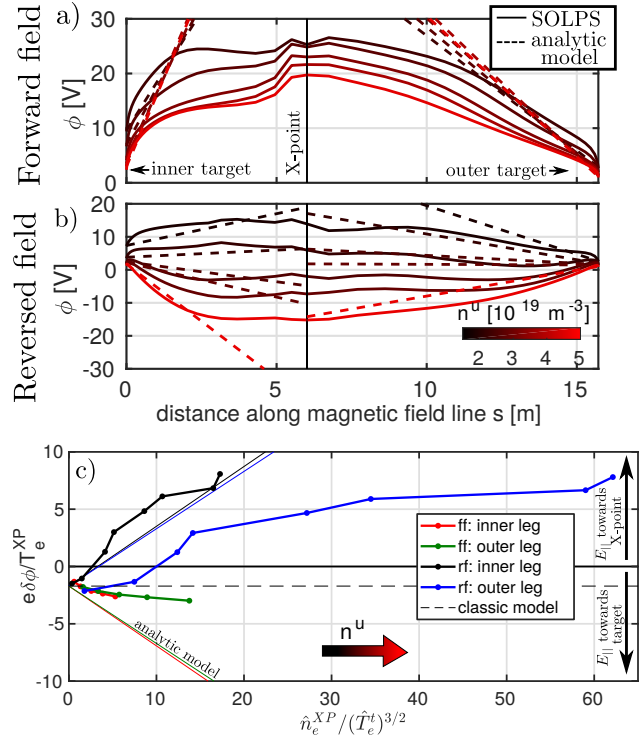
Figure 4. Comparison between model prediction and SOLPS-ITER simulations. ϕ profile along the flux tube adjacent to the separatrix in the PFR a) forward field b) reversed field and c) potential well depth $\delta\phi$ as function of normalized density $\hat{n}_e^{XP} = n_e^{XP}/10^{19}$ m^{-3} and temperature $\hat{T}_e = T_e^t/1\ eV$.

values by factors of up to 2-3 due to the simplified geometry (flux expansion is assumed constant along the leg), it correctly captures the sign of the electric field for both B_t directions (Figure 4a,b) and describes the potential drop $\delta\phi$ scaling with divertor conditions (Figure 4c).

|	inner leg	outer leg
poloidal leg length L_{XP}	21 cm	37 cm
divertor leg angle α	14.0°	74.6°
$\lambda_j \approx 1$ cm$\times f_{exp}^t$	1.0 cm	2.3 cm
$|B/B_\theta|$	9.7	15.7
resulting $m/sign(B_t)$	0.52	0.50

Table 2. Geometric parameters in the simulated geometry and resulting slope m for the potential well depth scaling.

3. Implications for divertor particle transport

3.1. Poloidal particle transport

We now investigate the effect of the potential well on divertor particle transport for the main plasma species D^+ by first considering the transport in the poloidal direction. High-density cases with fixed transport coefficients in forward and reversed field ($n_u \approx 3.8 \cdot 10^{19}$ m^{-3}, $T_e^{t,peak} = 0.5...2$ eV) are compared. The poloidal particle flux may be written as $\Gamma_\theta = \Gamma_\theta^{||} + \Gamma_\theta^{E \times B} + \tilde{\Gamma}_\theta^{dia} + \Gamma_\theta^{An}$, with $\Gamma_\theta^{||} = \frac{B_\theta}{B} n_{D^+} v_{D^+}^{||}$ where $v_{D^+}^{||}$ is the parallel velocity of D^+ ions obtained from the momentum balance, i.e. containing components of transport not directly related to drift effects. Again, only the non-divergence-free part of the diamagnetic flux is considered as the divergence-free part is largely related to the superposition of gyro-motions that does not lead to guiding-center displacements and hence does not contribute to particle transport perpendicular to the magnetic field [1]. The poloidal anomalous particle flux $\Gamma_\theta^{An} = -D_\perp^{An} \partial_\theta n_{D^+}$ is small w.r.t. the parallel and $E \times B$ fluxes and not considered in the following . The simulation indicates that the parallel component dominates poloidal particle transport in the divertor region in forward field (Figure 5 a), whereas $E \times B$ adds a minor contribution that follows the classical drift pattern (Figure 5 b). The same holds for low density cases in reversed field where $\Gamma_\theta^{E \times B}$ and Γ_θ^{dia} are, as expected, reversed (not shown). For the high density reversed field configuration, strong E_r close to the separatrix, related to the potential well, leads to locally $E \times B$-dominated transport in this, approximately 1 cm wide, layer (Figure 5 e). Here, the flow direction opposes the classical

drift direction and becomes comparable to the parallel flux.
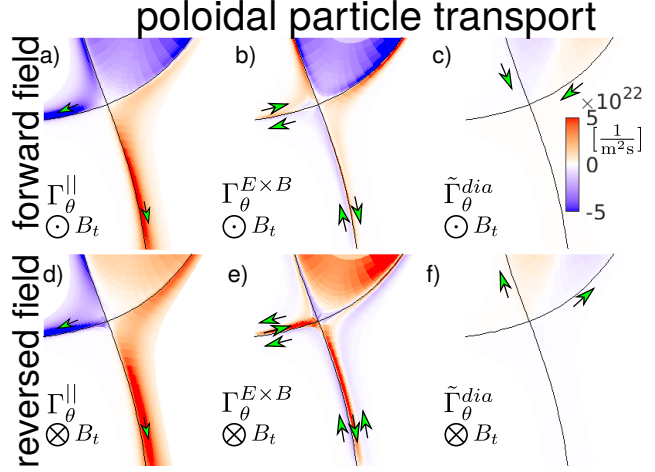
Figure 5. Relative contribution of parallel, $E \times B$ and diamagnetic fluxes to poloidal particle transport. Red/blue indicate transport towards the outer/inner targets, respectively. Although the parallel component typically dominates, $E \times B$ contributes significantly in presence of a potential well.
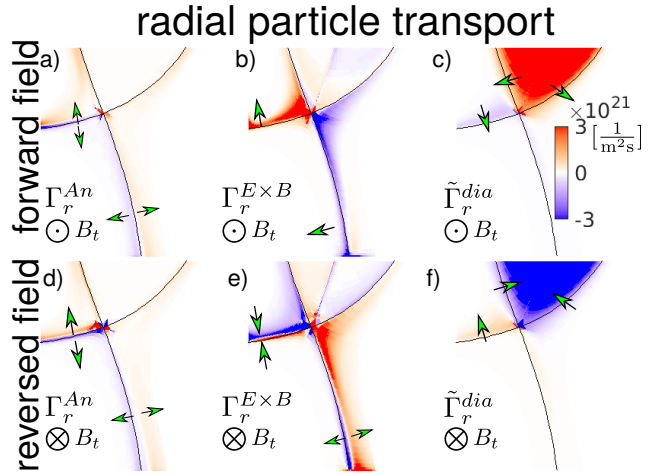
Figure 6. Relative contribution of anomalous, $E \times B$ and diamagnetic fluxes to radial particle transport. Red/blue indicate transport radially outwards/inwards, respectively. Cross-field transport in the divertor is $E \times B$-dominated for both B_t directions.

3.2. Radial particle transport

The radial particle flux is decomposed as $\Gamma_r = \Gamma_r^{An} + \Gamma_r^{E \times B} + \tilde{\Gamma}_r^{dia}$, where $\Gamma_r^{An} = -D_\perp^{An} \partial_r n_{D^+}$ is the anomalous cross-field particle flux, assumed diffusive, as a simple ansatz to describe cross-field turbulent fluxes. The diffusivity $D_\perp^{An} = 0.2$ m²/s is assumed constant as a physics basis for its spatial dependence is still lacking. This choice, however, leads to an upstream scrape-off layer width similar to typical TCV L-mode discharges $\lambda_n \sim 1$ cm. Turbulence simulations often indicate that cross-field flows are strongest upstream on the low field side [28], so this anomalous diffusivity probably overestimates the anomalous transport in the divertor. Despite this, the simulated radial transport in the divertor volume is found to be dominated by $E \times B$-flow, as reported previously [4]. This leads to a radially shifted density profile at the outer target of ~ 1 cm, mapped upstream, between forward and reversed B_t direction. In forward field, the radial $E \times B$ flux follows the classic drift direction, that, again, reverses for low density reversed field cases (not shown). In high-density reversed field cases, however, a radial compression of the inner (and widening of the outer) leg is found due to the opposite sign of $E_{\parallel}$ in the private and common flux regions (Figure 6e). The commonly accepted notion that drift directions simply reverse with B_t does not necessarily hold, here, for detached divertor conditions.

4. Conclusions

In reversed field the formation of an electric potential well is observed in SOLPS-ITER single null TCV simulations for low temperature divertor conditions. This well is a consequence

of divertor Pfirsch-Schlüter currents, i.e. when parallel and diamagnetic currents provide the main contributions to the charge balance. A proposed analytic model describes the dependencies on field direction and the emergence of the potential well during a density ramp and predicts a scaling of the well depth with divertor geometry, density and temperature. The presence of a potential well causes a substantially altered particle flux when compared to the classic drift pattern. The simulated poloidal component is found to be typically dominated by the parallel flux, while a potential well can cause significant $E \times B$-related transport in the near-SOL region. In the radial direction, the simulations indicate $E \times B$-dominated particle transport for TCV even in presence of turbulent transport, resulting in a radial shift of the target density profile with respect to the separatrix. A potential well also leads to radial compression/widening of the inner/outer divertor legs, respectively. The significant changes in divertor flows in presence of the predicted potential well may strongly influence divertor performance for plasma operation in reversed B_t, e.g. for operation in I-mode or reverse triangularity plasmas. The results presented herein are, however, not limited to single null configurations as in double null configurations one of the two X-points has the required ∇B-direction, regardless of the field direction B_t, to exhibit a potential well [29].

[1] A. Chankin, J. Nucl. Mater. 241-243, 199-213, 1997

[2] T.D. Rognlien et al., J. Nucl. Mater. 266-269, 654-659, 1999

[3] V. Rozhansky, Contrib. Plasma Phys. 58, 540-546, 2018

[4] A. Jaervinen, Nucl. Mater. Energy 12, 1136-1140, 2017

[5] I. Seninchenkov et al., Plasma Phys. Control. Fusion 61, 045013, 2019

[6] F. Ryter et al 2013 Nucl. Fusion 53 113003

[7] H. Du et al., J. Nucl. Mater. 463, 485-488, 2015

[8] H. Du et al., Plasma Phys. Control. Fusion 58, 085006, 2016

[9] W. Dekeyser et al., Nucl. Mat. and En. 12, 899-907, 2017

[10] G.D.Porter et al., Phys. of Plasmas 17, 112501, 2010

[11] F. Reimold et al., Nucl. Mater. Energy 12, 193-199, 2017

[12] N.Christen et al., Plasma Phys. Control. Fusion 59, 105004, 2017

[13] I. Seninchenkov et al., FIP/2, EX/2, TH/2 / 909, Study of detached H-modes in full tungsten ASDEX Upgrade with N seeding by SOLPS-ITER modeling, 2016

[14] A. Jaervinen et al., Phys. Rev. Let. 121, 075001, 2018

[15] M. Schaffer et al., J. Nucl. Mater. 290-293, 2001

[16] F.L. Hinton, Y.-B. Kim, Nucl. Fusion 34, 899, 1994

[17] *Proceedings of the 36th EPS Conference on Plasma Physics*, Sofia, P1.150, 2009

[18] Schneider, et al., Contr. Plasma Phys. 46, 1-191, 2006

[19] M. Schaffer et al., Nucl. Fusion 37, 83, 1997

[20] S. Wiesen, et al., J. Nucl. Mater. 463, 480-484, 2015

[21] X. Bonnin, et al., Plasma Fusion Res. 11, 1403103, 2016

[22] E. Kaveeva, et al., Nucl. Fusion 58, 126018, 2018

[23] J. Loizu et al., J. Plasma Phys 83, 575830601, 2017

[24] F. Halpern, P. Ricci, arXib:1606.085641v1

[25] M. Wensing, et al., Plasma Phys. Contr. Fus. 61, 085029, 2019

[26] M. Wensing et al., *Proceedings of the 46th EPS Conference on Plasma Physics*, Milan, P5.1043, 2019

[27] G.M. Staebler, F.L. Hinton, Nucl. Fusion 29, 10, 1989

[28] A. Gallo et al., Plasma Phys. Contr. Fusion 60, 014007, 2017

[29] E. Vekshina et al., Plasma Phys. Control. Fusion 61, 125009, 2019